Journal of the Optical Society of America A
OPTICS, IMAGE SCIENCE, AND VISION

Compositional prior information in computed infrared spectroscopic imaging

Bradley Deutsch,[1] Rohith Reddy,[1,2,3] David Mayerich,[1] Rohit Bhargava,[1,4,5] and P. Scott Carney[1,4,*]

[1]The Beckman Institute for Advanced Science and Technology, University of Illinois at Urbana-Champaign, Urbana, Illinois 61801, USA
[2]Department of Bioengineering, University of Illinois at Urbana-Champaign, Urbana, Illinois 61801, USA
[3]Wellman Center for Photomedicine, Massachusetts General Hospital and Harvard Medical School, Boston, Massachusetts 02114, USA
[4]Department of Electrical and Computer Engineering, University of Illinois at Urbana-Champaign, Urbana, Illinois 61801, USA
[5]Departments of Mechanical Science and Engineering, Chemical and Biomolecular Engineering, and Chemistry, University of Illinois at Urbana-Champaign, Urbana, Illinois 61801, USA
*Corresponding author: carney@illinois.edu

Received 4 February 2015; revised 7 April 2015; accepted 7 April 2015; posted 21 April 2015 (Doc. ID 231676); published 13 May 2015

Compositional prior information is used to bridge a gap in the theory between optical coherence tomography (OCT), which provides high-resolution structural images by neglecting spectral variation, and imaging spectroscopy, which provides only spectral information without significant regard to structure. A constraint is proposed in which it is assumed that a sample is composed of N distinct materials with known spectra, allowing the structural and spectral composition of the sample to be determined with a number of measurements on the order of N. We present a forward model for a sample with heterogeneities along the optical axis and show through simulation that the N-species constraint allows unambiguous inversion of Fourier transform interferometric data within the spatial frequency passband of the optical system. We then explore the stability and limitations of this model and extend it to a general 3D heterogeneous sample.

OCIS codes: (300.0300) Spectroscopy; (180.0180) Microscopy; (100.3200) Inverse scattering.

http://dx.doi.org/10.1364/JOSAA.32.001126

1. INTRODUCTION

Optical measurements of an unknown sample are affected by the real and imaginary parts of its refractive index. The problem of how to decouple these influences was first addressed by Fourier transform refractometry, in which the complex refractive index is estimated for a homogeneous slab [1,2]. The subsequently developed optical coherence tomography (OCT) [3–7] and microscopic spectroscopy [8–10] have found a wide range of applications in medicine, biology, and material science. In each, broadband light is focused at multiple positions in a sample, and elastically scattered light is collected through interferometric measurements, which are used to reconstruct aspects of the sample.

In OCT, it is assumed that the object is composed of a single material, and a measurement yields a spatially dependent density of the sample. In infrared spectroscopic imaging and microscopy [11], the density of the object is ignored within the focal volume, and a measurement yields the spatially dependent spectral response. In most heterogeneous samples, the density and spectral response vary, which is apparent in the measurements [12–14]. In this paper, we propose an "N-species" constraint, in which the object is assumed to be composed of a finite number of materials, each with a known spectral response. We show that, by taking interferometric data using focused, broadband light at multiple focal planes, such an object can be reconstructed unambiguously.

2. SPECTRAL–SPATIAL COUPLING

Spectral measurements of an object are affected by its spatially dependent density and the bulk spectral response of its composite materials. The structure of the sample causes diffraction, which can significantly influence the spectral response and is regarded as a confounding effect [12,13,15]. Nonetheless, it is possible to collect enough independent data to determine the spatially dependent density and spectrum of an object. We have previously demonstrated, for example, that the measured spectra can be successfully predicted using a rigorous solution of Maxwell's equations formulated in a coupled-wave picture [14]. An inversion of such a forward model would require diffraction-limited sampling along all three spatial dimensions and would have large computational complexity. As the dimensionality and number of species composing an object grow, the required data sets are correspondingly larger, resulting in more expensive computation.

Several strategies for recovering separate spatial and structural information from OCT-like measurements have been

developed. The short-time Fourier-transform [16–21], wavelet-transform [22], Wigner–Ville [23], and dual-window [24,25] methods are able to recover spatially dependent spectra. In these methods, it is assumed that the structure varies slowly such that its spatial frequencies are outside the optical bandwidth recorded or do not overlap with the spectral features of the sample. They imply a well-known trade-off among spatial resolution, spectral resolution, and spectral accuracy. For a detailed comparison, see [26].

Here, we propose a strategy in which we do not make assumptions about the spatial bandwidth but, instead, on the composition of the object. In particular, we assume that the sample is composed of a finite number N of spectrally distinct species with known bulk spectral response. We use this prior information to reduce the size of the data set required to retrieve full chemical and structural information under the first Born approximation. This can be seen as a special case of the partial separability assumption used to take advantage of sparsity in magnetic resonance spectroscopic imaging and other spatiotemporal imaging modalities [27,28].

A forward model is constructed for scattering, propagation, and measurement for a sample in an interferometric imaging experiment. We consider for simplicity a sample with inhomogeneities only along the propagation axis. The model is inverted using a number of measurements on the order of N to recover the object. We investigate the stability of the inversion with respect to various experimental parameters, as well as the particular spectral responses of the sample.

3. FORWARD MODEL

The sample is presumed to be located in one arm of an asymmetric Fourier-transform infrared spectroscopic microscope, as illustrated in Fig. 1. Light from a broadband source is split into the two interferometer arms and recombined on the detector, resulting in an interferometric measurement. The reference mirror is translated along the optical axis to change the optical path difference linearly in time, resulting in a sampled time-dependent signal (inset of Fig. 1) whose complex discrete Fourier transform is influenced by the absorption spectrum of the sample and also the phase acquired on scattering. As in OCT, the full complex field is, thus, determined at the detector for each sample position. The size of the focal spot dictates the lateral spatial resolution of the instrument and is limited by diffraction to approximately half the center wavelength of the source, on the order of 1–10 μm for mid-IR sources.

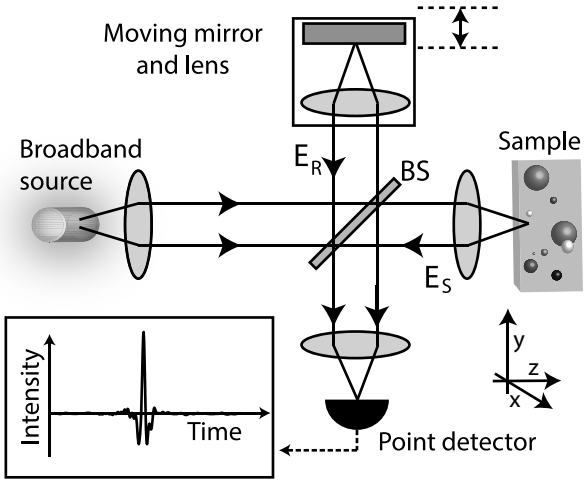

Fig. 1. Presumed experimental setup. Light from a mid-IR source is focused on the sample, which can be moved in three dimensions. The scattered light is combined with a reference field in a Michelson interferometer. The reference mirror moves to generate a sampled centerburst as a function of time at the point detector.

The sample is described by a linear optical susceptibility $\eta(\mathbf{r}, k_0)$, which may be thought of as the projection of an object vector $|\eta\rangle$ onto the spatial–spectral basis element $\langle \mathbf{r}, k_0|$ and is a function of sample coordinate $\mathbf{r}$ and the free-space wave vector $k_0 = 2\pi/\lambda$, where λ is the wavelength.

The measurement set is represented by $S(\mathbf{k}_\parallel, k_0, z_F) = \langle \mathbf{k}_\parallel, k_0, z_F|S\rangle$ and can be described approximately as the result of a linear operation on the sample:

$$\langle \mathbf{k}_\parallel, k_0, z_F|S\rangle \approx \langle \mathbf{k}_\parallel, k_0, z_F|\mathbf{KW}|\eta\rangle, \tag{1}$$

where we have parameterized the measurement by the wave vector magnitude $k_0 = |\mathbf{k}|$, the position of the focus along the z axis z_F, and the transverse Fourier component $\mathbf{k}_\parallel$. The linear operators $\mathbf{W}$ and $\mathbf{K}$ describe an intensity weighting due to the focus and the interferometric measurement, respectively. As previously reported [29], they can be evaluated asymptotically and written as

$$\mathbf{W} = \int \mathrm{d}^2\mathbf{k}_\parallel \, \mathrm{d}k_0 \, \mathrm{d}z \sum_{z_F} |\mathbf{k}_\parallel, k_0, z, z_F\rangle \tag{2}$$

$$\times W(\mathbf{k}_\parallel, k_0, z, z_F)\langle \mathbf{k}_\parallel, k_0, z|, \tag{3}$$

where

$$W(\mathbf{k}_\parallel, k_0, z, z_F) = \frac{4\pi^3 U_0(k_0)\tilde{g}^2(\mathbf{k}_\parallel/2, k_0)}{|z - z_F| + z_R}, \tag{4}$$

and

$$\mathbf{K} = \int \mathrm{d}^2\mathbf{k}_\parallel \, \mathrm{d}k_0 \, \mathrm{d}z \sum_{z_F} |\mathbf{k}_\parallel, k_0, z_F\rangle \tag{5}$$

$$\times e^{-2ik_z(\mathbf{k}_\parallel/2)(z-z_F)}\langle \mathbf{k}_\parallel, k_0, z, z_F|. \tag{6}$$

Here, z is the coordinate along the propagation direction, $U_0(k_0)$ is the source amplitude as a function of wavenumber, $\tilde{g}$ is the normalized transverse beam shape in Fourier space, which we take as a zero-order Gaussian: $\tilde{g} = \exp(-\mathrm{NA}^2|\mathbf{k}_\parallel|^2/2\pi k_0^2)$, $z_R = 2/(k_0\,\mathrm{NA}^2)$ is the Rayleigh range, w_0 is the beam waist, and the longitudinal component of the wave vector is related to the transverse component by $k_z = \sqrt{k^2 - |\mathbf{k}_\parallel|^2}$. We note that $\tilde{g}$ need not be Gaussian but may be any square-integrable function in Fourier space. Acting on $|\eta\rangle$ with $\mathbf{KW}$ produces an intensity at the detector, which must then be sampled to make a measurement. To that end, we introduce a sampling operator $\mathbf{D}$: $L_2(\mathbb{R}^3) \times \mathbb{R}^{N_z} \to l_2(\mathbb{Z}^3) \times \mathbb{R}^{N_z}$, defined as

$$\mathbf{D} = \int \mathrm{d}k_0 \, \mathrm{d}^2\mathbf{k}_\parallel \sum_{\boldsymbol{\kappa}_\parallel, \boldsymbol{\kappa}, z_F} |\boldsymbol{\kappa}_\parallel, \boldsymbol{\kappa}, z_F\rangle D(\mathbf{k}_\parallel, k_0)\langle \mathbf{k}_\parallel, k_0, z_F|, \tag{7}$$

where $\boldsymbol{\kappa}$ (with $|\boldsymbol{\kappa}| = \kappa$) and $\boldsymbol{\kappa}_{\|}$ are wave-vector components defined on a sampling grid, rather than continuous parameters, and $D(\mathbf{k}_{\|}, k_0)$ is a sampling function. In the simplest case, we can choose $D = \delta(k_0 - \kappa)\delta(\mathbf{k}_{\|} - \boldsymbol{\kappa}_{\|})$, representing the process of sampling instantaneously on a discrete, evenly spaced lattice. The summation over $\boldsymbol{\kappa}$ in Eq. (7) is over the range $[\boldsymbol{\kappa}_{\min}, \boldsymbol{\kappa}_{\max}]$, which is, in turn, dictated by the position resolution of the reference mirror.

This model works under the first Born approximation and uses scalar Gaussian fields. It, thus, fails in cases of high sample contrast or high numerical aperture. We also assume that the autocorrelation terms in the interference measurement can be neglected. For a discussion of the effect of these terms and their removal, see [30,31].

A. Single Species, 1D Heterogeneous Object

First, we consider the case of a sample heterogeneous object only in the principal direction of light propagation, such that $|\eta_{1d}\rangle = \delta(\mathbf{k}_{\|})|\eta\rangle$, where δ is the Dirac delta function. Then, our estimate of the object is given by

$$|\tilde{\eta}\rangle = (\mathbf{D}_{1d}\mathbf{K}_{1d}\mathbf{W}_{1d})^{+}|S\rangle, \tag{8}$$

where the + superscript denotes the Moore–Penrose pseudoinverse, and the operators above reduce in the 1D case to

$$\mathbf{W}_{1d} = \int \mathrm{d}k_0\, \mathrm{d}z \sum_{z_F} |k_0, z, z_F\rangle W_{1d}(k_0, z, z_F)\langle k_0, z|, \tag{9}$$

$$\mathbf{K}_{1d} = \int \mathrm{d}k_0\, \mathrm{d}z, : \sum_{z_F} |k_0, z_F\rangle e^{-2ik_0(z-z_F)}\langle k_0, z, z_F|, \tag{10}$$

and

$$\mathbf{D}_{1d} = \int \mathrm{d}k_0 \sum_{\boldsymbol{\kappa}, z_F} |\boldsymbol{\kappa}, z_F\rangle D(\boldsymbol{\kappa})\langle k_0, z_F|, \tag{11}$$

where

$$W_{1d}(k_0, z, z_F) = \frac{4\pi^3 U_0(k_0)}{|z - z_F| + z_R}. \tag{12}$$

Here, we have used the fact that $k_z|_{\mathbf{k}_{\|}=0} = k_0$.

In OCT/interferometric synthetic aperture microscopy (ISAM), the susceptibility is implicitly taken as separable, such that $|\eta\rangle = |\rho\rangle|f\rangle$ and $\langle \mathbf{r}, k_0\rangle\eta = \langle \mathbf{r}\rangle\rho\langle k_0\rangle f = \rho(\mathbf{r})f(k_0)$. That is, the sample consists of a single species with spectral response f as a function of wavenumber k_0, and spatial density variation ρ as a function of spatial coordinate $\mathbf{r}$. The spectral response is typically estimated from a known sharp feature of the sample (e.g., a planar interface). Figures 2(a) and 2(b) are simulated demonstrations of OCT under these conditions. In (a), the z-dependent density of a single-species object is plotted as a function of depth. A measurement is produced using the matrix $\mathbf{D}_{1d}\mathbf{W}_{1d}\mathbf{K}_{1d}$ assuming a numerical aperture (NA) of 0.5 and three foci, equally spaced throughout the depth of the object. In (b), the density of the sample is retrieved. Here, and, in subsequent results, Tikhonov regularization is used, such that the pseudoinverse of an operator is given by $\mathbf{G}^{+} = (\mathbf{G}^{*}\mathbf{G} + \epsilon\mathbf{I})\mathbf{G}^{*}$, where $= \mathbf{I}$ is the identity operator and ϵ is a constant. A discrete fast Fourier transform is used to compute the Fourier transform.

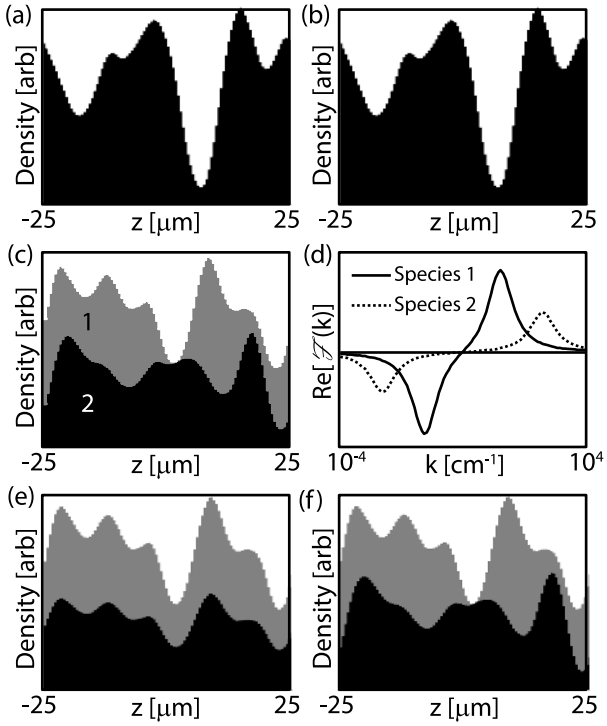

Fig. 2. Comparison of OCT with and without compositional prior information. (a) Density profile of a single-species object. (b) OCT-type regularized inversion for single-species object, in which it is assumed that we have knowledge of its spectral response. (c) Density profile of a two-species object. (d) Real parts of the spectral responses of species 1 and 2. (e) OCT-type regularized inversion of two-species object, in which we are missing information about the spectral response of species 2. The inversion reconstructs the total density profile but assigns equal weight to each species at each depth. (f) Retrieved regularized density with full spectral information, as provided by the N-species constraint. The individual densities of species 1 and 2 are retrieved as well as the total density.

B. Multispecies, 1D Heterogeneous Object

We now consider a special class of objects known to be composed of a limited number of species with different absorption spectra, so that the susceptibility can be represented as $\langle \mathbf{r}, k_0\rangle\eta = \sum_{j=1}^{N} \rho_j(\mathbf{r}) f_j(k_0)$. In Fig. 2(c), the simulated sample is composed of a mixture of two species with complex Lorentzian spectra, given by

$$f_n(k_0) \propto \frac{\bar{k}_n^2 - k_0^2}{(\bar{k}_n^2 - k_0^2)^2 + k_0^2\gamma^2} + \frac{i\gamma k_0}{(\bar{k}_n^2 - k_0^2)^2 + k_0^2\gamma^2}, \tag{13}$$

where $\bar{k}$ is the center wavenumber and γ is a damping constant. Moreover, we assume that the f_j's are linearly independent. The $N \times M$ matrix formed by the spectral functions (M being the number of spectral points) needs to be full rank, so it is implicitly assumed that $M > N$, i.e., the number of spectral points collected is at least as many as the number of species.

The real parts of these spectra for two species are plotted in Fig. 2(d). Figure 2(e) shows the result of applying an OCT-type inversion scheme in which only the spectrum of species 1 is known. The total density of the object is recovered but not the individual densities of each species. Since we have no way to

distinguish species 1 from species 2, the Tikhonov-regularized solution assigns equal density to each species.

We now apply compositional prior information by defining $|\eta\rangle = \mathbf{M}|P\rangle$, where the compositional operator,

$$\mathbf{M}_{1d} = \sum_{z,j} |k_0, z\rangle f_j(k_0) \langle z, j|, \tag{14}$$

acts on the object, now represented as a vector parameterized by position and species index, $P(z, j) = \langle z, j|P\rangle$, with $j \in (1, N)$. The spectral response of species j is described by the complex function of wavenumber, $f_j(k_0)$.

For a number of foci N_F at different sample locations, we have a well-posed problem in the noiseless case, within the spatial-frequency passband of the optical instrument. Inverting the operator $\mathbf{H}_{1d} = \mathbf{D}_{1d}\mathbf{K}_{1d}\mathbf{W}_{1d}\mathbf{M}_{1d}$ and acting on the measurement $|S\rangle$ yields the object estimate shown in Fig. 2(f). The density of each species is retrieved accurately, in addition to the total density.

Figure 3 illustrates two examples of density retrieval with prior compositional information. In Fig. 3(a), the density profile of smooth sample, including five species, is shown. Inverting $\mathbf{H}_{1d}$ results in the retrieved density profile shown in Fig. 3(b). Another commonly encountered geometry in OCT and spectroscopy is that of a layered sample, in which the composite material types may be known. Figure 3(c) shows an example of the density profile of such a sample, in which the density has been chosen to be identical at all z positions, but the species index varies. The retrieved density is shown in Fig. 3(d). The correct densities and species indices are retrieved, with some noise in the inversion due to numerical instabilities.

C. Limiting Cases

In the limit that the sample is composed of a single species (plus vacuum), we have $N = 1$. The density vector becomes $|P_1\rangle = \delta_{j1}|P\rangle$, where δ_{1j} is the Kronecker delta function, equal to 1 at species index $j = 1$ and 0 elsewhere. For a single focal position, the measurement is described by

$$|S_1\rangle \propto \sum_{z,k_0} |k_0\rangle \frac{e^{2ik(z-z_f)} f_1(k_0)}{|z - z_F| + z_R} \langle z|P_1\rangle, \tag{15}$$

which is the standard OCT/ISAM problem in one dimension. In practice, f_1 may be estimated from the data by identifying a sharp feature in the sample. An example of this situation is shown in Figs. 2(a) and 2(b).

In the other extreme, the sample may have a completely unknown, spatially dependent spectral response. If the sample is parameterized by N_k spectral bins at each position z, we can project it on a basis such that

$$F(k_0) = \sum_{i=1}^{N_k} f_i \delta_{k_0,k_i}. \tag{16}$$

This represents the limiting case of spectroscopic microscopy. Generally, the result of such a measurement is assumed to approximate the spectral response at each pixel, such that $\langle k_0, \mathbf{r}|S\rangle \approx \langle k_0, \mathbf{r}|P\rangle$, but the structure of the object influences the measurement through scattering. Our model accounts for this effect in the single-scattering limit.

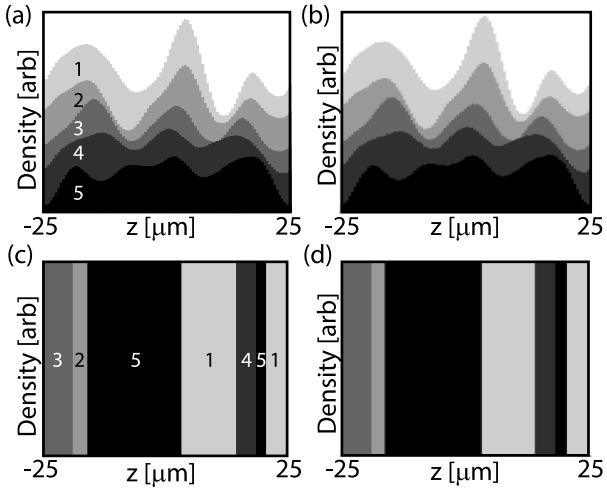

Fig. 3. Examples of inversions with compositional prior information. (a) Smooth sample density as a function of z, with five species. (b) Inversion using compositional prior information and data from 10 foci. (c) Layered sample density as a function of z, with five species. (d) Inversion using compositional prior information and data from 15 foci.

4. DISCUSSION

A. Stability and Condition Number of the Operator KWM

In the noiseless case, we are able to retrieve the object within the spatial-frequency passband of the instrument (high spatial frequencies are lost due to the limiting aperture or the diffraction limit cannot be recovered). However, the stability of the inversion is sensitive to many parameters, including the number of species and foci, the NA corresponding to the focus, and the particular spectral behavior of the species. Figure 4 is a summary of trends in the stability of the inversion in the absence of regularization. In Fig. 4(a), a density plot is shown of the log of the condition number, C, of $\mathbf{G}_{1d}^{+}$ as a function of the number of species N, and foci N_F with other parameters fixed to those used in Fig. 2(f). The condition number indicates the stability of the result with respect to small changes in the measurement, with lower C corresponding to a more stable inversion. For $N_F < N$, the problem is ill-posed (i.e., the matrix is singular), and more foci provide redundant information, leading to a more stable inversion. Similarly, Fig. 4(b) shows how C varies with respect to the NA of the system. As the NA approaches zero, the "focus" becomes a plane wave, and it is impossible to retrieve the structure. As the NA increases, the stability improves. For very high NA (not shown), there is significant dark space between the foci, resulting in a loss of information and decreased stability. Note that this model is only strictly applicable to low NA, but this analysis captures the basic stability characteristics of the model as the NA increases.

One important tool used in the stability of linear inversions is the Gramian matrix, which quantifies correlations among the vectors on which the object is projected. In the spatially homogeneous case, the normal operator $\mathbf{M}^*\mathbf{M}$ is equal to the Gramian matrix of the system. The condition number, therefore, results directly from the degree of similarity among the

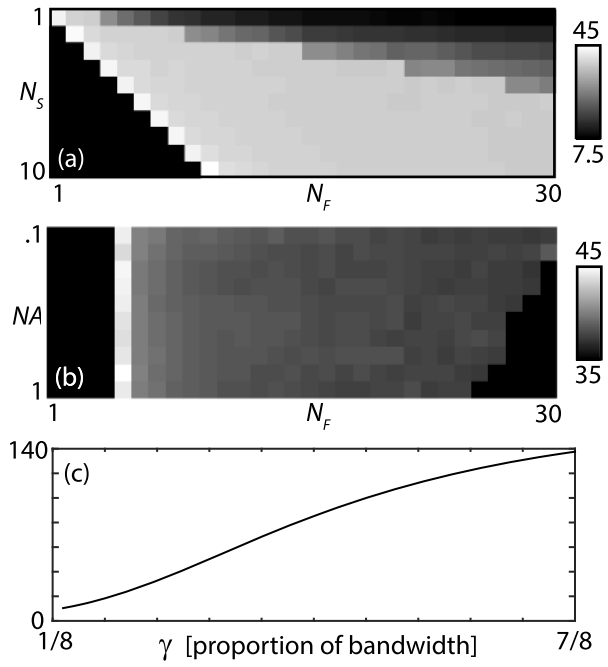

Fig. 4. Density plots of $\log(C)$. (a) $\log(C)$ versus number of species N_s and number of foci N_F. The inversion becomes less stable with more species and more stable with more foci. (b) $\log(C)$ versus NA and number of foci. Increasing the NA leads to a more stable inversion. (c) Condition number of $(\mathbf{M}^*\mathbf{M})^+$ versus spectral width γ, given as a proportion of the full bandwidth. As the spectra become wider they overlap, leading to a less stable inversion.

spectra as well as the total signal strength. Figure 4(c) shows the condition number of $(\mathbf{M}^*\mathbf{M})^+$ for a spatially homogeneous sample composed of a mixture of five species with complex Lorentzian spectra as a function of the spectral width. As the width changes from 1/8 to 7/8 of the spectral bandwidth, the spectra begin to overlap significantly, which leads to a higher condition number and less stable inversion. As the spectral width decreases, the stability improves until there is significant space between the spectral peaks. Note that, if we were free to choose an orthonormal basis of spectral functions, $\mathbf{M}^*\mathbf{M}$ would be diagonal, maximizing the stability of the inversion.

B. 3D Samples

The linear model above is extended easily for a 3D object. We simply define an operator $\mathbf{M}$ analogous to that in Eq. (14),

$$\mathbf{M} = \sum_{\mathbf{k}_\parallel, z, j} |\mathbf{k}_\parallel, k_0, z\rangle f_j(k_0) \langle \mathbf{k}_\parallel, z, j|, \tag{17}$$

and insert $\mathbf{M}|P\rangle = |\eta\rangle$ into Eq. (1) such that $\mathbf{H} = \mathbf{DKWM}$. Inverting $\mathbf{H}|P\rangle$ now requires N measurements for each component of $\mathbf{k}_\parallel$. This can be accomplished, for example, by raster scanning at each of N different focal planes. The inversion process is identical, but the computational cost is large. The matrix represented by $\mathbf{H}$ has $N_f \cdot N_{k_x} \cdot N_{k_y} \cdot N_k$ rows and $N \cdot N_{k_x} \cdot N_{k_y} \cdot N_k$ columns. For an object sampled on a cubic grid of side M pixels with the minimum number of foci ($N_F = N$) and no prior information regarding the spatial frequency spectrum, the complexity of such a matrix inversion scales with a lower bound of $\mathcal{O}\{(M^3 \cdot N_k)^{2.37}\}$ in the most optimistic case for a general matrix [32] but may be faster if the matrix symmetries in this problem were exploited.

5. CONCLUSIONS

We have considered a linear model for spatial–spectral optical measurements in which it is known that the sample consists of a number of known species and found that the problem is well posed in the noise-free case, as long as the number of foci is equal to or greater than the number of species. In the extreme cases of single-species objects and complete ignorance, we find the standard cases of OCT/ISAM and spectroscopic microscopy, respectively. This work, thus, bridges a theoretical gap between the two.

Beckman Postdoctoral Fellowship.

REFERENCES

1. S. G. Kaplan, L. M. Hanssen, U. Griesmann, and R. Gupta, "Fourier transform refractometry," Proc. SPIE **3425**, 203–212 (1998).
2. C. Saloma, V. Darla, and J. Muñoz, "Fourier transform refractometry using multichannel detection," Appl. Opt. **32**, 4785–4789 (1993).
3. D. Huang, E. A. Swanson, C. P. Lin, W. G. Stinson, W. Chang, R. Hee, T. Flotte, K. Gregory, C. A. Puliafito, and J. G. Fujimoto, "Optical coherence tomography," Science **254**, 1178–1181 (1991).
4. B. E. Bouma and J. G. Tearny, *The Handbook of Optical Coherence Tomography* (Marcel Dekker, 2001).
5. C. Puliafito, M. Hee, C. Lin, E. Reichel, J. Schuman, J. S. Duker, J. A. Izatt, E. A. Swanson, and J. G. Fujimoto, "Imaging of macular diseases with optical coherence tomography," Opthalmology **102**, 217–229 (1995).
6. J. Schmitt, A. Knuttel, M. Yadlowsky, and M. Eckhaus, "Optical-coherence tomography of a dense tissue—statistics of attenuation and backscattering," Phys. Med. Biol. **39**, 1705–1720 (1994).
7. S. A. Boppart, B. E. Bouma, C. Pitris, J. F. Southern, M. E. Brezinski, and J. G. Fujimoto, "In vivo cellular optical coherence tomography imaging," Nat. Med. **4**, 861–865 (1998).
8. P. Colarusso, L. H. Kidder, I. W. Levin, J. C. Fraser, J. F. Arens, and E. N. Lewis, "Infrared spectroscopic imaging: from planetary to cellular systems," Appl. Spectrosc. **52**, 106A–120A (1998).
9. E. N. Lewis, P. J. Treado, R. C. Reeder, G. M. Story, A. E. Dowrey, C. Marcott, and I. W. Levin, "Fourier transform spectroscopic imaging using an infrared focal-plane array detector," Anal. Chem. **67**, 3377–3381 (1995).
10. M. J. Nasse, M. J. Walsh, E. C. Mattson, R. Reininger, A. Kajdacsy-Balla, V. Macias, R. Bhargava, and C. J. Hirschmugl, "High-resolution Fourier-transform infrared chemical imaging with multiple synchrotron beams," Nat. Methods **8**, 413–416 (2011).
11. R. Bhargava, "Infrared spectroscopic imaging: the next generation," Appl. Spectrosc. **66**, 1091–1120 (2012).
12. R. Bhargava, S.-Q. Wang, and J. L. Koenig, "FT-IR imaging of the interface in multicomponent systems using optical effects induced by differences in refractive index," Appl. Spectrosc. **52**, 323–328 (1998).
13. J. Lee, E. Gazi, J. Dwyer, M. D. Brown, N. W. Clarke, J. M. Nicholson, and P. Gardner, "Optical artifacts in transflection mode FTIR microspectroscopic images of single cells on a biological support: the effect of back-scattering into collection optics," Analyst **132**, 750–755 (2007).
14. B. J. Davis, P. S. Carney, and R. Bhargava, "Theory of midinfrared absorption microspectroscopy: I. homogeneous samples," Anal. Chem. **82**, 3474–3486 (2010).
15. R. Reddy, B. Davis, P. Carney, and R. Bhargava, "Modeling Fourier transform infrared spectroscopic imaging of prostate and breast cancer tissue specimens," in *IEEE International Symposium on Biomedical Imaging: From Nano to Macro* (IEEE, 2011), pp. 738–741.

16. C. Xu, J. Ye, D. L. Marks, and S. A. Boppart, "Near-infrared dyes as contrast-enhancing agents for spectroscopic optical coherence tomography," Opt. Lett. **29**, 1647–1649 (2004).
17. N. Bosschaart, M. C. Aalders, D. J. Faber, J. J. Weda, M. J. Van Gemert, and T. G. Van Leeuwen, "Quantitative measurements of absorption spectra in scattering media by low-coherence spectroscopy," Opt. Lett. **34**, 3746–3748 (2009).
18. N. Bosschaart, D. J. Faber, T. G. van Leeuen, and M. C. G. Aalders, "In vivo low-coherence spectroscopic measurements of local hemoglobin absorption spectra in human skin," J. Biomed. Opt. **16**, 100504 (2011).
19. N. Bosschaart, D. J. Faber, T. G. van Leeuwen, and M. C. G. Aalders, "Measurements of wavelength dependent scattering and backscattering coefficients by low-coherence spectroscopy," J. Biomed. Opt. **16**, 030503 (2011).
20. J. Yi and V. Backman, "Imaging a full set of optical scattering properties of biological tissue by inverse spectroscopic optical coherence tomography," Opt. Lett. **37**, 4443–4445 (2012).
21. C. P. Fleming, J. Eckert, E. F. Halpern, J. A. Gardecki, and G. J. Tearney, "Depth resolved detection of lipid using spectroscopic optical coherence tomography," Biomed. Opt. Express **4**, 1269–1284 (2013).
22. U. Morgner, W. Drexler, F. X. Kärtner, X. D. Li, C. Pitris, E. P. Ippen, and J. G. Fujimoto, "Spectroscopic optical coherence tomography," Opt. Lett. **25**, 111–113 (2000).
23. R. N. Graf and A. Wax, "Temporal coherence and time frequency distributions in spectroscopic optical coherence tomography," J. Opt. Soc. Am. A **24**, 2186–2195 (2007).
24. F. E. Robles, C. Wilson, G. Grant, and A. Wax, "Molecular imaging true-colour spectroscopic optical coherence tomography," Nat. Photonics **5**, 744–747 (2011).
25. F. Robles, R. N. Graf, and A. Wax, "Dual window method for processing spectroscopic optical coherence tomography signals with simultaneously high spectral and temporal resolution," Opt. Express **17**, 6799–6812 (2009).
26. N. Bosschaart, T. G. van Leeuwen, M. C. G. Aalders, and D. J. Faber, "Quantitative comparison of analysis methods for spectroscopic optical coherence tomography," Biomed. Opt. Express **4**, 2570–2584 (2013).
27. Z.-P. Liang, "Spatiotemporal imaging with partially separable functions," in *4th IEEE International Symposium on Biomedical Imaging: From Nano to Macro* (ISBI, 2007), pp. 988–991.
28. H. M. Nguyen, X. Peng, M. N. Do, and Z.-P. Liang, "Denoising MR spectroscopic imaging data with low-rank approximations," IEEE Trans. Biomed. Eng. **60**, 78–89 (2013).
29. A. Ahmad, N. Shemonski, S. G. Adie, H. Kim, W.-M. W. Hwu, P. S. Carney, and S. Boppart, "High-speed interferometric synthetic aperture microscopy on a graphics processing unit," in *Frontiers in Optics 2012/Laser Science XXVIII*, OSA Technical Digest (online) (Optical Society of America, 2012), p. FM4D.2.
30. B. J. Davis, T. S. Ralston, D. L. Marks, S. A. Boppart, and P. S. Carney, "Autocorrelation artifacts in optical coherence tomography and interferometric synthetic aperture microscopy," Opt. Lett. **32**, 1441–1443 (2007).
31. V. M. Gelikonov, G. V. Gelikonov, D. A. Terpelov, D. V. Shabanov, and P. A. Shilyagin, "Suppression of image autocorrelation artefacts in spectral domain optical coherence tomography and multiwave digital holography," Quantum Electron. **42**, 390–393 (2012).
32. V. V. Williams, "Multiplying matrices faster than Coppersmith-winograd," in *Proceedings of the Forty-fourth Annual ACM Symposium on Theory of Computing, STOC '12* (ACM, 2012), pp. 887–898.